AGU PUBLICATIONS

JGR

Journal of Geophysical Research: Solid Earth

RESEARCH ARTICLE
10.1002/2014JB011502

Key Points:
- Analysis of the 1992-2010 ground deformation via the SBAS DInSAR technique
- Two macro-areas of deformation are recurrently active in Yellowstone caldera
- Caldera unrest is probably caused by a combination of magma and fluid migration

Supporting Information:
- Tables S1–S3
- Table S1
- Table S2
- Table S3
- Appendices S1 and S2

Correspondence to:
P. Tizzani,
tizzani.p@irea.cnr.it

Citation:
Tizzani, P., M. Battaglia, R. Castaldo, A. Pepe, G. Zeni, and R. Lanari (2015), Magma and fluid migration at Yellowstone Caldera in the last three decades inferred from InSAR, leveling, and gravity measurements, *J. Geophys. Res. Solid Earth*, *120*, 2627–2647, doi:10.1002/2014JB011502.

Received 29 JUL 2014
Accepted 3 FEB 2015
Accepted article online 11 FEB 2015
Published online 6 APR 2015

Magma and fluid migration at Yellowstone Caldera in the last three decades inferred from InSAR, leveling, and gravity measurements

P. Tizzani[1], M. Battaglia[2,3], R. Castaldo[1], A. Pepe[1], G. Zeni[1], and R. Lanari[1]

[1]Istituto per il Rilevamento Elettromagnetico dell'Ambiente (IREA-CNR), Naples, Italy, [2]Department of Earth Sciences, Sapienza University of Rome, Rome, Italy, [3]U.S. Geological Survey, Volcano Science Center, Menlo Park, California, USA

Abstract We studied the Yellowstone caldera geological unrest between 1977 and 2010 by investigating temporal changes in differential Interferometric Synthetic Aperture Radar (InSAR), precise spirit leveling and gravity measurements. The analysis of the 1992–2010 displacement time series, retrieved by applying the SBAS InSAR technique, allowed the identification of three areas of deformation: (i) the Mallard Lake (ML) and Sour Creek (SC) resurgent domes, (ii) a region close to the Northern Caldera Rim (NCR), and (iii) the eastern Snake River Plain (SRP). While the eastern SRP shows a signal related to tectonic deformation, the other two regions are influenced by the caldera unrest. We removed the tectonic signal from the InSAR displacements, and we modeled the InSAR, leveling, and gravity measurements to retrieve the best fitting source parameters. Our findings confirmed the existence of different distinct sources, beneath the brittle-ductile transition zone, which have been intermittently active during the last three decades. Moreover, we interpreted our results in the light of existing seismic tomography studies. Concerning the SC dome, we highlighted the role of hydrothermal fluids as the driving force behind the 1977–1983 uplift; since 1983–1993 the deformation source transformed into a deeper one with a higher magmatic component. Furthermore, our results support the magmatic nature of the deformation source beneath ML dome for the overall investigated period. Finally, the uplift at NCR is interpreted as magma accumulation, while its subsidence could either be the result of fluids migration outside the caldera or the gravitational adjustment of the source from a spherical to a sill-like geometry.

1. Introduction

The Yellowstone volcanic field was formed by three giant caldera-forming eruptions that occurred around 2.1, 1.3, and 0.64 Ma in and around Yellowstone National Park, WY, the most recent one responsible for the 60 km wide and 40 km long Yellowstone caldera. Two structural resurgent domes formed after the last caldera-forming eruption: the Mallard Lake (ML) resurgent dome in the southwestern region of Yellowstone caldera and the Sour Creek (SC) resurgent dome in the northeast part of the caldera (Figure 1). In the last 0.64 Ma, at least 30 rhyolitic lava flows have covered the caldera floor, while basalt has erupted outside the caldera to the north in the Norris-Mammoth corridor and to the south in the Island Park area [*Christiansen,* 2001]. During the Holocene, the caldera has experienced alternating episodes of subsidence and uplift [*Pierce et al.,* 2002]. A widespread hydrothermal system with over 10,000 geysers, hot springs, and fumaroles reflects the extraordinarily high convective ground water circulation. *Fournier* [1989] interpreted these processes as the effect of water circulation along fractures heated by crystallizing magma.

Investigations on deformation of the Yellowstone caldera region, performed by using precise leveling, Global Positioning System (GPS), and differential Interferometry Synthetic Aperture Radar (InSAR) interferograms [*Puskas et al.,* 2007; *Vasco et al.,* 2007; *Dzurisin et al.,* 2012, and references therein], have revealed the existence of cycles of inflation and deflation [e.g., *Wicks et al.,* 2006; *Puskas et al.,* 2007; *Chang et al.,* 2007, 2010; *Aly and Cochran*, 2011] and the migration of deformation from one resurgent dome to the other [*Wicks et al.,* 1998]. Deformation rates have significantly changed during the years. For example, the average subsidence (−) or uplift (+) rate of the caldera floor ranged between -3.5 ± 0.5 cm/yr and $+2.3 \pm 0.1$ cm/yr until 2004 and increased to $+5.3 \pm 0.3$ cm/yr during the 2004–2007 time interval [*Puskas et al.,* 2007; *Vasco et al.,* 2007; *Chang et al.,* 2007, 2010; *Dzurisin et al.,* 2012].

For what concerns the gravity measurements, the earliest observations and related inversions were presented by *Smith et al.* [1978]. *Arnet et al.* [1997] reported a Bouguer gravity increase during a period of uplift (1977–1983),

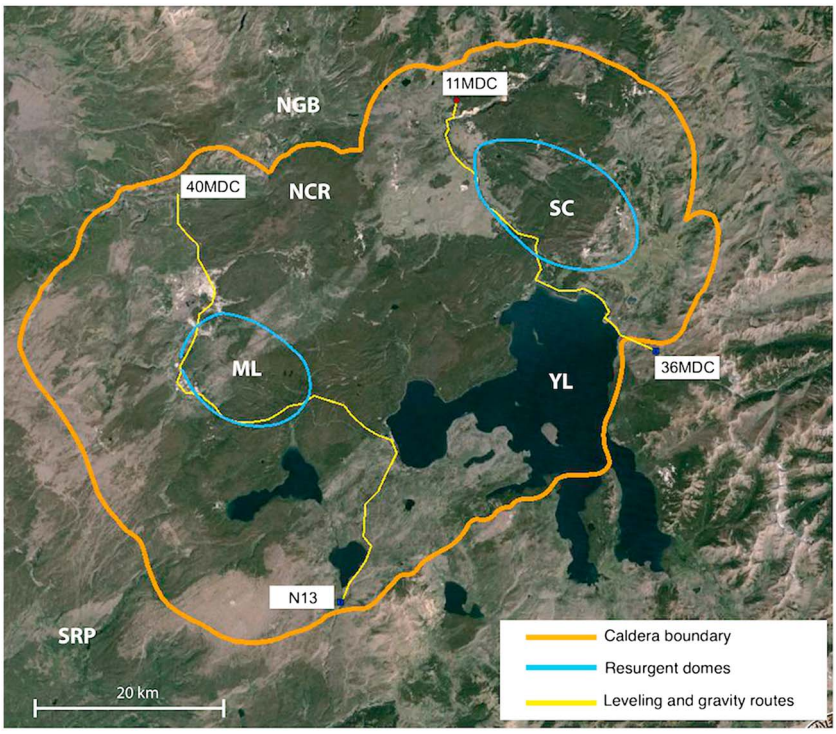

Figure 1. Landsat image of Yellowstone Caldera. In the map two macroareas are highlighted: the Mallard Lake (ML) and Sour Creek (SC) resurgent domes and a region close to the Northern Caldera Rim (NCR), about 10 km south of Norris Geyser Basin (NGB). Moreover, we also indicate the Snake River Plane (SRP) and the Yellowstone Lake (YL) zones. N13: base station of the Madison Junction-West Thumb Junction leveling line; 36MDC: base station of the Canyon Junction-Fishing Bridge Junction leveling line [*Dzurisin et al.,* 2012].

followed by little or no Bouguer gravity change during a period of subsidence (1986–1993). *Vasco et al.* [1990] modelled deformation (from 1976 to 1986) and temporal gravity variation (from 1977 to 1987) along a northwestern profile of the northern Yellowstone Caldera from Canyon Junction to Lake Butte Junction (Figure 1). The two data sets consisted of 13 observations each. Because of the limited station distribution along a single profile, *Vasco et al.* [1990] were not able to determine a specific model either for the volume or mass change but they were able to infer that the volume increase for the northern caldera source must lie above 9.0 km and involved a relative density perturbation greater then +20 kg/m^3.

Two general classes of models have been proposed to explain surface deformation at Yellowstone Caldera: "hydrothermal" or "magmatic" models. Hydrothermal models rely mainly on pressurization/depressurization of fluids other than magma to produce surface uplift/subsidence. The primary deformation mechanism is a pressure change within the hydrothermal system in response to some perturbation such as a gas/fluid pulse. Hydrothermal models invoke either a (1) supercritical fluid formed by phase separation from crystallizing magma and trapped beneath a self-sealing layer at lithostatic pressure in ductile rock to produce uplift; episodic rupturing of the seal would produce subsidence [e.g., *Fournier,* 1989] or (2) poroelastic deformation in the shallow hydrothermal system induced by magmatic gas influx at the base of the hydrothermal system [e.g., *Dzurisin et al.,* 1999; *Hutnak et al.,* 2009]. Furthermore, the hydrothermal model implies that (1) the depth of the sources should be above the brittle-ductile transition zone—that in Yellowstone is at a depth between 4 and 6 km under the resurgent domes area [*DeNosaquo et al.,* 2009]—and that (2) their density should be $\rho \leq 1000$ kg/m^3. The hydrothermal model is similar to the conceptual model employed to explain the deformation at the Campi Flegrei Caldera located in Southern Italy [e.g., *Battaglia et al.,* 2006].

The primary deformation mechanism for magmatic models is injection of magma or fluid exsolved from magma at or below the base of the hydrothermal system (i.e., depth below the brittle-ductile transition zone and density around 2500 kg/m^3). Inversion of GPS and/or InSAR and/or leveling measurements from *Wicks et al.* [2006], *Puskas et al.* [2007], *Vasco et al.* [2007], *Chang et al.* [2007, 2010], and *Aly and Cochran* [2011]

Journal of Geophysical Research: Solid Earth

10.1002/2014JB011502

Table 1. Results From Previous Modeling of Deformation[a]

Deformation			Source					
Period	Type	Data	Location	Geometry	Depth (km)	Volume change (km^3)	Cause of Unrest	Reference
1923–1977	Uplift	Leveling	Sour Creek dome	Tabular	4.5 ± 1.5	~0.37	magma and/or hydrothermal fluids	*Vasco et al.* [1990]
			Mallard Lake dome	Tabular	~9	~0.41	magma and/or hydrothermal fluids	
1976–1986	Uplift till 1984 Subsidence from 1984	Leveling	Sour Creek and Mallard Lake domes	Lens like	7.5 ± 2.5		magma and/or hydrothermal fluids	*Dzurisin et al.* [1994]
1985–1987	Subsidence	Leveling + trilateration	Sour Creek dome	Tabular	10 ± 5	−0.019 ± 0.002	magma and/or hydrothermal fluids	*Dzurisin et al.* [1990]
1992–1995	Subsidence	InSAR, GPS and leveling	Sour Creek and Mallard Lake domes	Tabular	8 ± 2	n/a	magma and faults	*Vasco et al.* [2007]
1993–1995	Subsidence	InSAR	Sour Creek dome	Tabular	~8	n/a	magma and/or hydrothermal fluids	*Wicks et al.* [1998]
			Mallard Lake dome	Tabular	8.5 ± 4.0	−0.046 ± 0.011	magma and/or hydrothermal fluids	
1996–2000	Uplift	InSAR, GPS and leveling	Sour Creek and Mallard Lake domes	Tabular	6 ± 2	n/a	magma and faults	*Vasco et al.* [2007]
1996–2002	Uplift	InSAR	Northern Caldera Rim	Tabular	17.5 ± 2.5	0.08 ± 0.02	magma	*Wicks et al.* [2006]
2004–2006	Subsidence	InSAR and GPS	Norris Geyser Basin	Tabular	11 ± 5	−0.010 ± 0.005	hydrothermal fluids	*Chang et al.* [2007]
	Uplift	InSAR and GPS	Sour Creek and Mallard Lake domes	Tabular	10 ± 4	0.22 ± 0.02	magma	
2005–2006	Subsidence	InSAR and GPS	Norris Geyser Basin	Point source	16.6	n/a	hydrothermal fluids	*Aly and Cochran* [2011]
	Uplift	InSAR and GPS	Sour Creek dome	Point source	10.4	n/a	magma	
	Uplift	InSAR and GPS	caldera floor between the resurgent domes	Tabular	13.1	0.03	magma	
	Uplift	InSAR and GPS	Mallard Lake dome	Point source	17.3	n/a	magma	
2005–2009	Subsidence	InSAR and GPS	Norris Geyser Basin	Tabular	10 ± 3	−0.06 ± 0.04	hydrothermal fluids	*Chang et al.* [2010]
	Uplift	InSAR and GPS	Sour Creek and Mallard Lake domes	Tabular	8 ± 1	0.32	magma	

[a]See Figure 1 for a map of the caldera.

identified either two or three subcaldera tabular bodies as the source of deformation: (1) one [e.g., *Chang et al.,* 2007] or two [e.g., *Wicks et al.,* 2006] bodies at a depth of 6–14 km beneath the caldera resurgent domes and (2) a source 8–16 km deep under the Northern Caldera Rim area. The microgravity observations by *Arnet et al.* [1997] are consistent with a "magmatic" model where surface uplift is caused, at least in part, by intrusion of magma in the midcrust, while subsidence is controlled by fluid loss from magma, e.g., either brine or gas. The source depths indicated by these and other models (see Table 1) are below the brittle-ductile transition—thought to occur at a depth between 4 and 6 km under the resurgent domes area [*DeNosaquo et al.,* 2009]—therefore, the assumption of linear elastic behavior could be violated in rock surrounding the deformation sources, adding additional uncertainties. To determine if viscoelastic processes are important or not in modeling the deformation, we can estimate the characteristic time τ for the viscoelastic relaxation of the crust beneath the resurgent domes. The delay time is given by $\tau = \eta/E$, where η is the crust viscosity and E its Young's modulus. According to *Puskas et al.* [2007], the viscosity of the viscoelastic lower crust in the Yellowstone Snake River plane is $\eta = 3 \pm 2 \times 10^{12}$ GPas. The caldera low-velocity zone (depth $\geq$8 km) has a density $\rho = 2900$ kg/m^3, and seismic velocities as low as $V_P \approx 4.6$ km/s and $V_P/V_S \approx 1.65$ beneath the resurgent domes [*Husen et al.,* 2004; *DeNosaquo et al.*, 2009], corresponding to a Young's module $E \approx 50$ GPa and a delay time $580 < \tau < 2900$ year. Since the delay time is much greater than the time range of the deformation cycles studied in this paper, we can neglect any contribution from viscoelastic processes. A similar conclusion is also reached by *Vasco et al.* [2007].

We present in this work the results of the analysis and inversion of InSAR, leveling, and gravity measurements relevant to the last three decades. In particular, we start by investigating the InSAR results obtained through the Small BAseline Subset (SBAS) differential InSAR technique [*Berardino et al.,* 2002], applied to a data set of European Remote-Sensing satellite (ERS)-1/2 and ENVISAT SAR images spanning 18 years, from 1992 to 2010. Moreover, we analyze the leveling data, which cover an additional time period of about 19 years from 1976 to 1995 [*Dzurisin et al.*, 2012], and the gravity measurements that span the interval from 1977 to 1993 [*Arnet*, 1996]. Parameters of the caldera best fitting deformation sources are inferred by inverting InSAR, leveling, and gravity measurements by using the dMODELS software package [*Battaglia et al.,* 2013].

Compared to previous work on Yellowstone Caldera (see Table 1), (i) we present long-term deformation time series derived from InSAR and their comparison to GPS results, (ii) we identify and remove the tectonic signal from the retrieved time-series, and (iii) we jointly exploit InSAR, leveling, and gravity measurements to investigate the deformation sources geometric characteristics and their densities; to do this we search for the best fit deformation source identified by inverting more than one source geometry, and we use statistical analysis to discriminate among different geometries.

Our study indicates the existence of different distinct deformation sources within the caldera, and we show that the detected sources have been intermittently active for the past three decades. We interpret the results of our inversions in view of the seismic tomography studies [*Husen et al.,* 2004; *Farrell et al.,* 2014]. This allows us to discriminate between the magmatic and the hydrothermal nature of the sources responsible for the unrest phenomena that affected the SC and ML resurgent caldera domes during the last three decades.

2. InSAR Measurements

2.1. InSAR Data Processing

To study the deformation signals affecting the Yellowstone caldera and its surroundings over almost two decades, we analyzed the SAR images collected by the ERS-1/2 and ENVISAT sensors of the European Space Agency (ESA) along descending orbits (Track 41, Frame 2709). In particular, we exploited 31 ERS-1/2 SAR images acquired from June 1992 to May 2007 and 22 ENVISAT images collected from May 2005 to September 2010 (see Table S1 in the supporting information). Satellite data were processed by using the SBAS differential InSAR technique [*Berardino et al.,* 2002; *Pepe et al.,* 2005; *Lanari et al.,* 2007].

Precise satellite orbital information and the three arc sec Digital Elevation Model (DEM) of the study area, obtained by the Shuttle Radar Topography Mission (SRTM) [*Rosen et al.,* 2001], were used to estimate the topographic phase components needed to compute the differential interferograms [*Franceschetti and Lanari*, 1999]. In addition, we applied a complex multilook operation [*Rosen et al.,* 2000], with four looks in the range

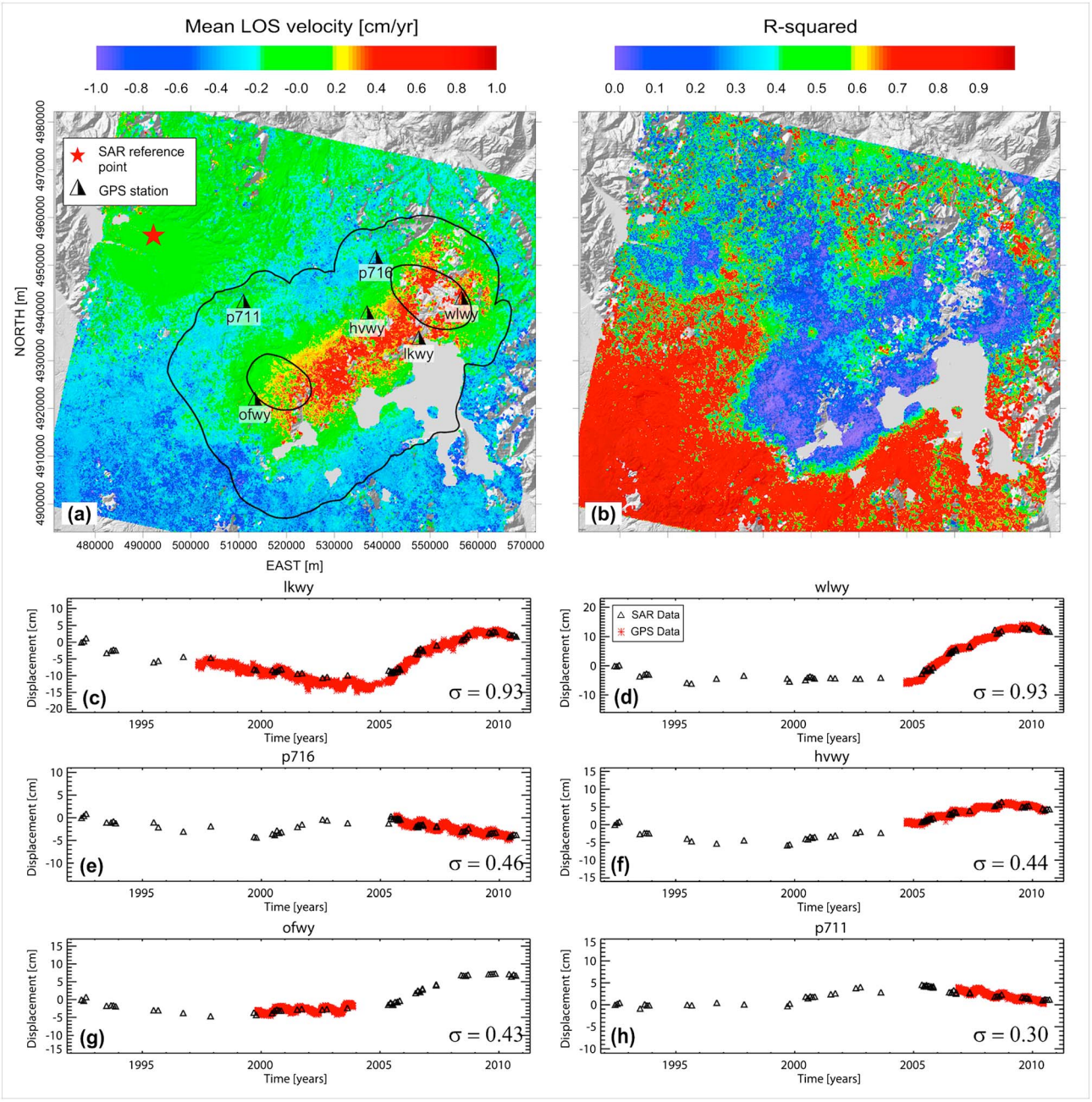

Figure 2. Differential InSAR data analysis. (a) Mean velocity map for the 1992–2010 time interval, superimposed to SRTM DEM of study area. The red star represents the reference point of the SBAS differential InSAR data processing. The black triangles indicate the location of GPS stations inside the caldera. The black solid lines represent the caldera and resurgent domes boundaries (see Figure 1). The radar azimuth angle is $\varphi \approx 189°$ and the incidence angle is $\lambda \approx 23°$. (b) Map of R squared for the 1992–2010 SBAS-InSAR deformation time series. (c–h) InSAR time series—measured at coherent pixels close to CGPS sites (black triangles)—compared to GPS displacement measurements projected along the radar Line Of Sight (LOS).

direction and twenty looks in the azimuth one, followed by an advanced multitemporal noise-filtering process [*Yang et al.,* 2013] to mitigate noise decorrelation effects [*Zebker and Villasenor,* 1992*; Bamler and Hartl,* 1998].

Following the generation of the noise-filtered interferograms, we have retrieved the original (unwrapped) phase signals from the measured (modulo 2π restricted) wrapped interferograms through phase unwrapping operation [*Fornaro et al.*, 1997a, 1997b; *Costantini*, 1998*; Goldstein et al.*, 1988]. In particular, this result has been achieved by using the Extended Minimum Cost Flow phase unwrapping approach [*Pepe and Lanari*, 2006]. Finally, we employed the SBAS differential InSAR

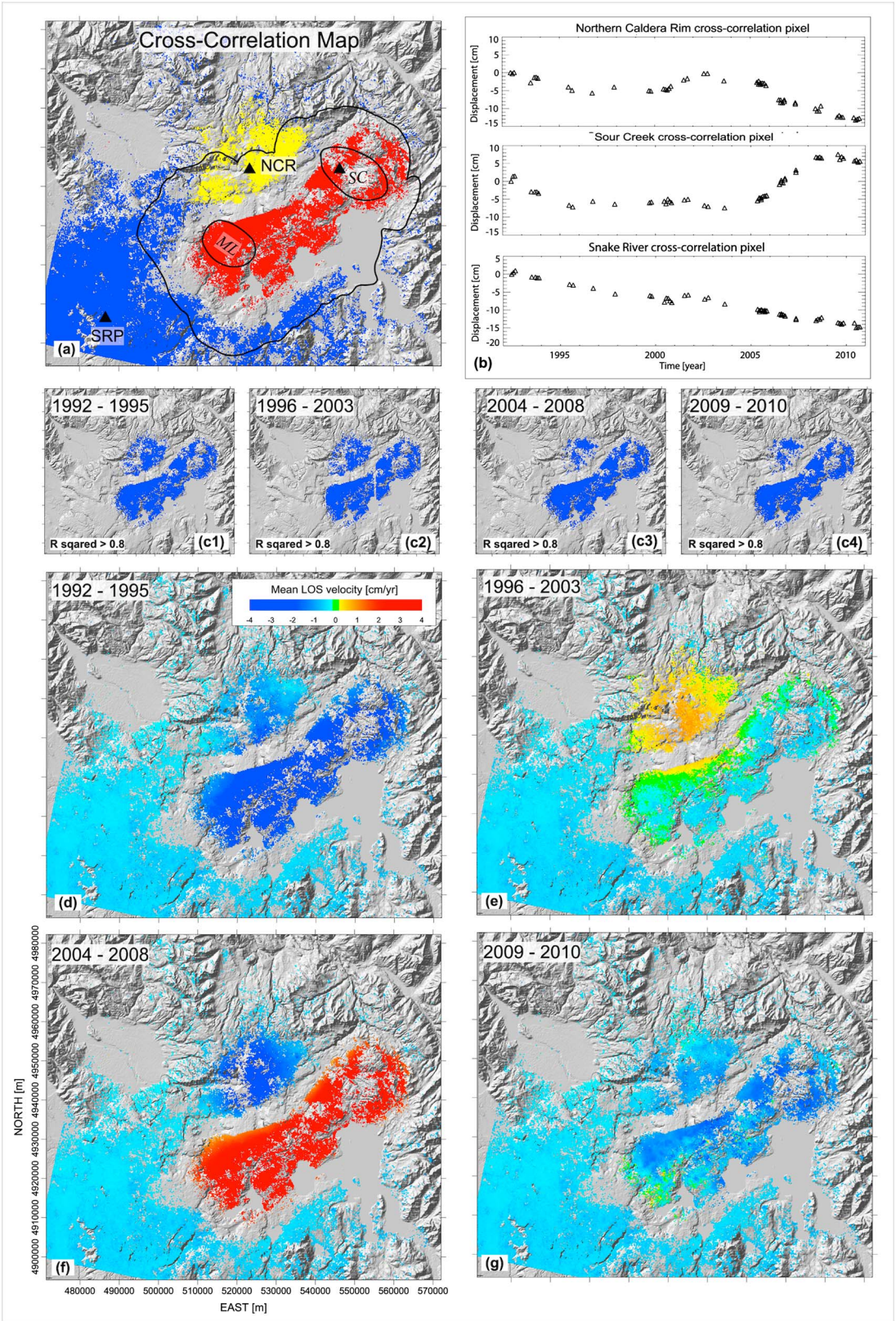

Figure 3. Cross-correlation analysis. (a) Cross-correlation map: the yellow, red, and blue points indicate the coherent cluster pixels derived by cross-correlation analysis. The black solid lines represent the caldera and resurgent domes boundaries (see Figure 1). (b) Deformation time series of the three selected SAR pixel (black triangles) employed in the cross-correlation analysis. (c1–c4) Scatter maps of the temporal and spatial linear behaviour. (d–g) Mean LOS velocity maps in different time interval.

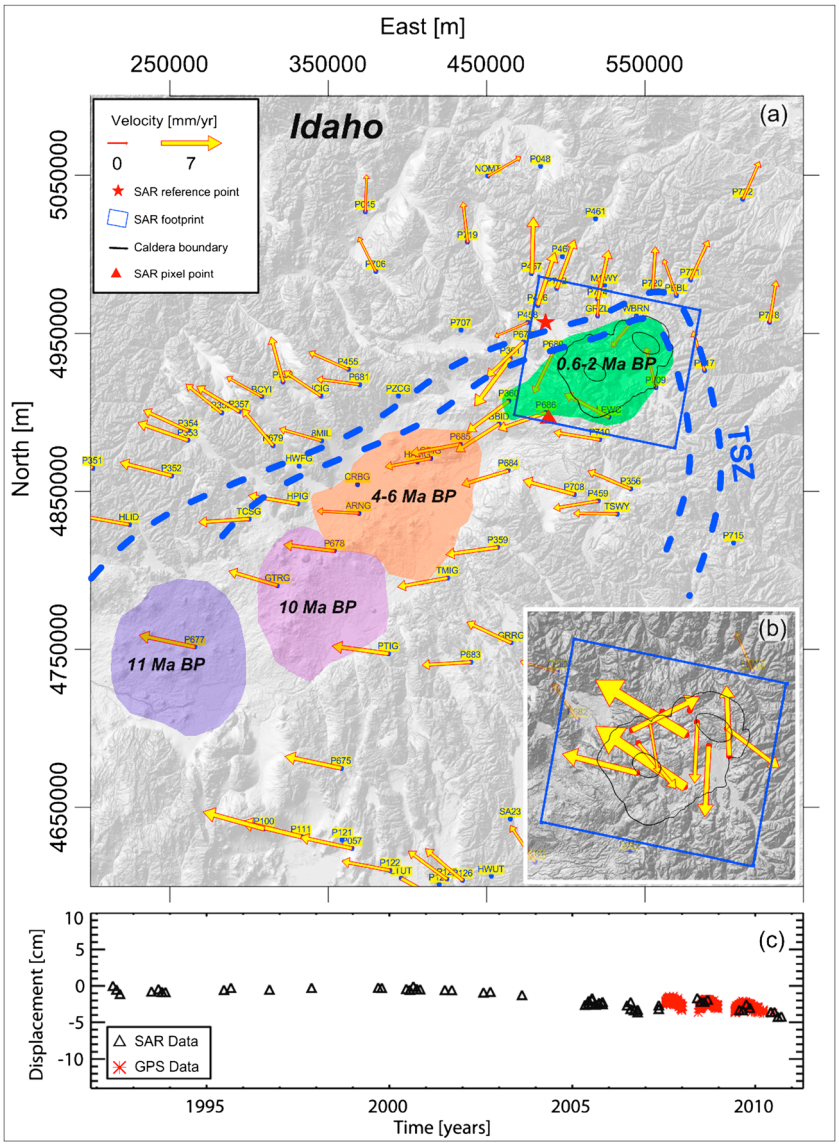

Figure 4. Regional and local deformation field. (a) CGPS deformation velocities [GPS data from the U.S. Geological Survey website http://earthquake.usgs.gov/monitoring/gps/]. The colored areas indicate the age of the volcanic processes. The Tectonic Seismic Zone represents the area where is concentrated the natural seismicity. The red star is the reference point of the SBAS differential InSAR data processing. (b) CGPS velocities inside caldera area. (c) Comparison between deformation at a pixel SAR, red triangle in Figure 4a and the nearest GPS stations (P686).

procedure to compute the 1992–2010 mean deformation velocity map and the corresponding displacement time series (Figure 2). It is worth noting that we excluded the pixels with low-accuracy measurements (incoherent points) characterized by low values of the temporal coherence factor [*Pepe and Lanari*, 2006].

All SBAS differential InSAR deformation measurements have been computed relative to one reference pixel assumed stable, located outside the caldera region (highlighted in Figure 2a by a red star). We compared the InSAR time series—measured at coherent pixels close to CGPS sites (black triangles in Figures 2c–2h)—to GPS displacement measurements projected along the radar Line Of Sight (LOS). The estimated values of the standard deviation difference between InSAR and GPS surface deformation is (on average) around 7 mm, consistent with other SBAS differential InSAR quality assessments focused on the use of ERS-1/2 and ENVISAT data [*Casu et al.*, 2006; *Bonano et al.*, 2012].

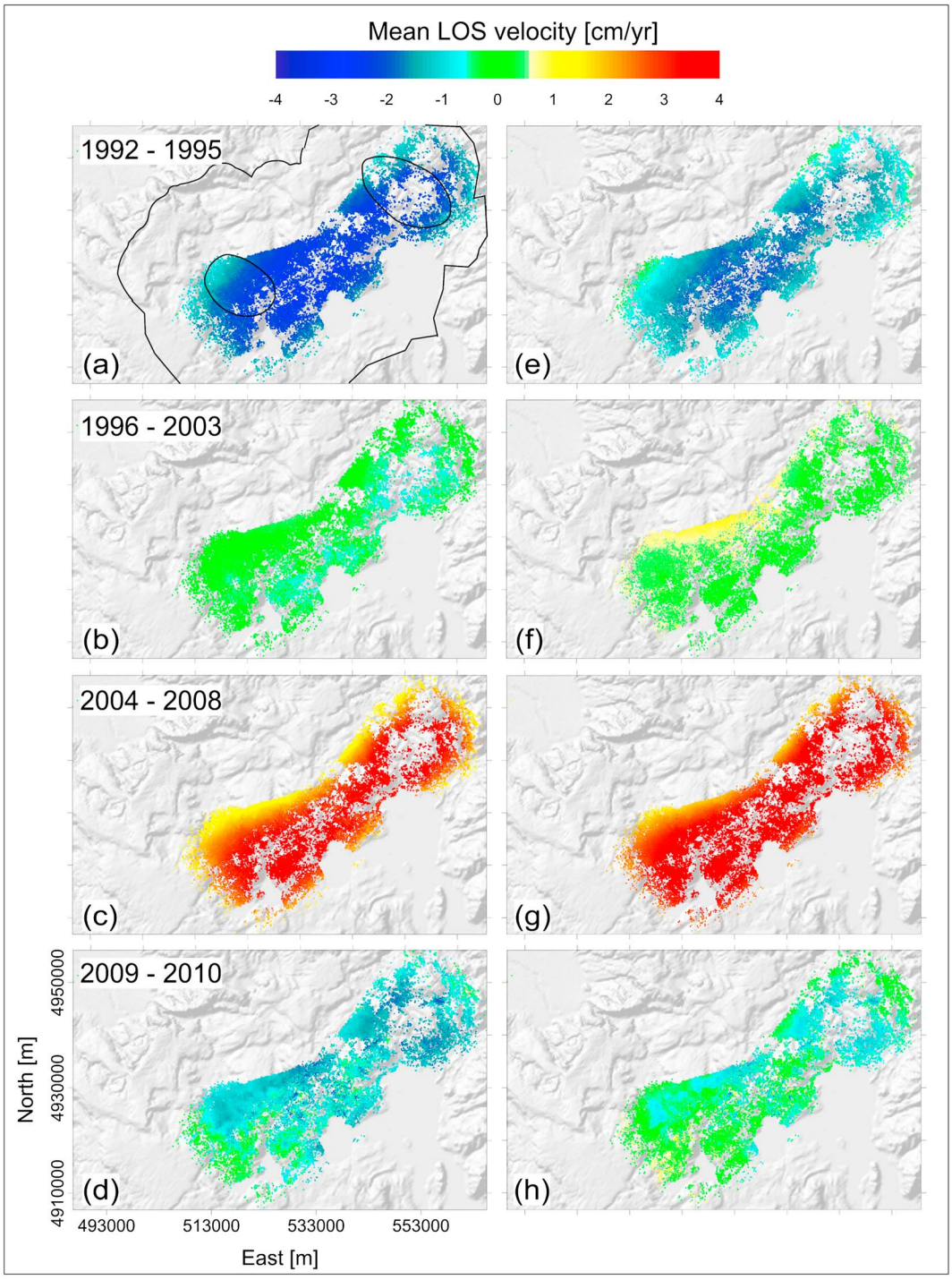

Figure 5. Differential InSAR analysis of the ML and SC resurgent domes. (a–d) Mean LOS deformation velocity map including regional North American (NA) Plate tectonic component. (e–h) Mean LOS deformation velocity after the removal the regional NA Plate tectonic component. In Figure 5a the black solid lines represent the caldera and resurgent domes boundaries (see Figure 1).

2.2. Areas of Significant Deformation

The analysis of the retrieved InSAR deformation time series reveals a multifaceted deformation scenario for the Yellowstone region. In particular, we can identify three different macroareas characterized by distinct deformation behaviors: (i) Mallard Lake (ML) and Sour Creek (SC) resurgent domes, (ii) Northern Caldera Rim (NCR), and

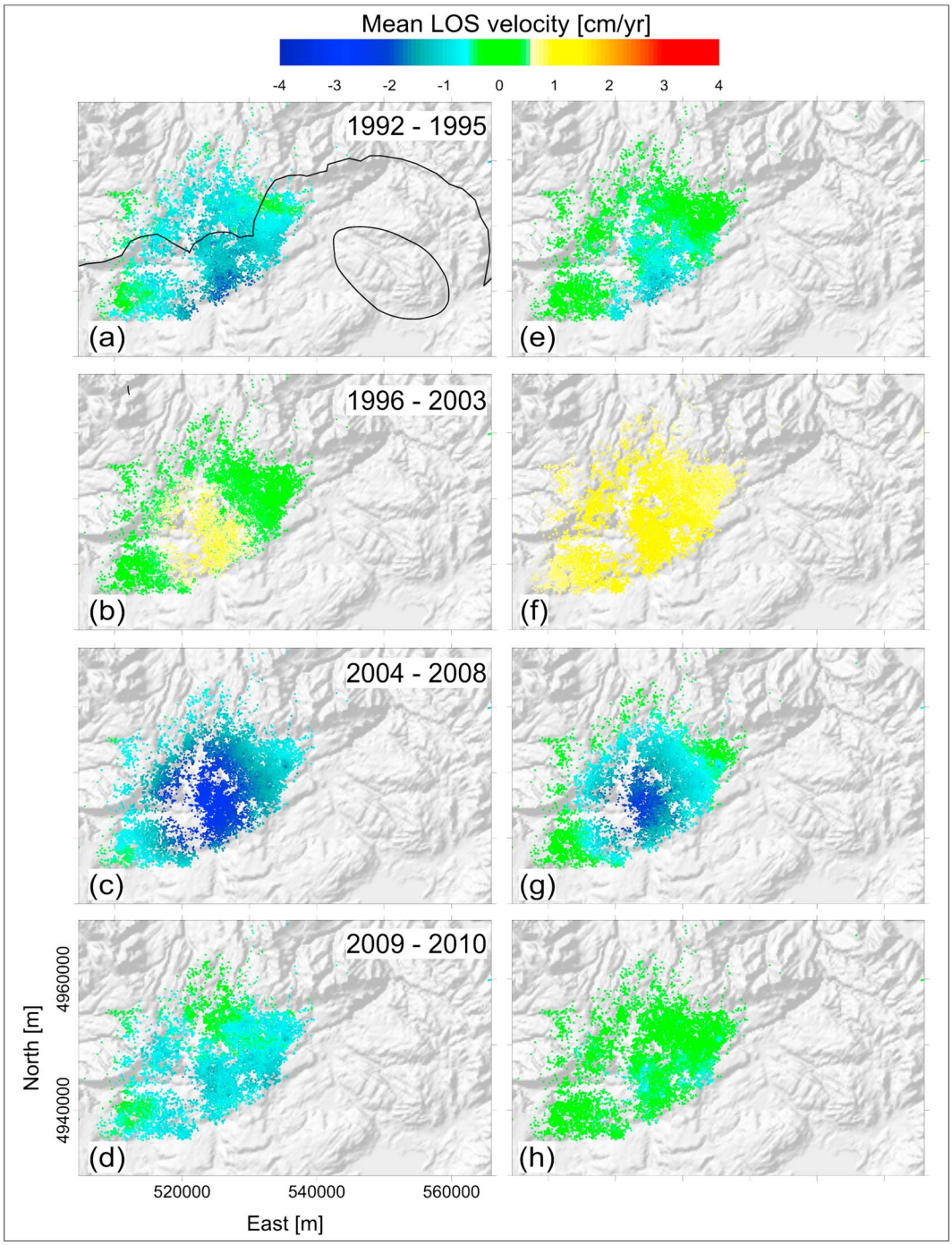

Figure 6. Differential InSAR analysis of the northern caldera rim. (a–d) Mean LOS deformation velocity map including regional North American (NA) plate tectonic component. (e–h) Mean LOS deformation velocity after the removal the regional NA plate tectonic component. In Figure 6a the black solid lines represent the caldera and resurgent domes boundaries (see Figure 1).

(iii) Snake River Plain (SRP). To minimize the influence of deformation sources not related to the same geophysical process, we selected for our analysis only those pixels whose time series had a correlation greater than 0.95 with pixels located in the zone of maximum deformation. For each of the identified macroareas, similarly to what was proposed in *Tizzani et al.* [2007], we selected a SAR pixel and computed the corresponding cross-correlation maps (see Figure 3a). We plot in Figure 3b the deformation time series for the three selected pixels (highlighted by black triangles in Figure 3a), derived from the above

Table 2. InSAR: Best Fit Sources for 1992–1995 (Figure 7a)[a]

							Residuals Analysis									
N	*P*	Area	Geometry	χ^2_ν	%	NRMSE 1 StD	Mean	R^2	*X* (UTM)	*Y* (UTM)	Depth (m)	ΔV (10^6 m^3)	Radius (m)	A	θ (deg)	φ (deg)
65.900	8	Mallard Lake	sphere	1.2	58	0.30	0.0007	0.93	528,701	4,923,143	15,441	−21				
		Sour Creek	sphere						549,344	4,936,719	14,199	−13				
65.900	*14*	*Mallard Lake*	*spheroid*	*0.8*	*68*	*0.23*	*0.0007*	*0.74*	*528,700*	*4,923,800*	*19,500*	*−27*		*0.30*	*8*	*145*
									±200	*±500*	*±2,800*	*±5*				
		Sour Creek	*spheroid*						*552,600*	*4,935,200*	*12,700*	*−10*		*0.3*	*48*	*310*
									±1,900	*±1,100*	*±1,000*	*±3*				
65.900	10	Mallard Lake	sill	1.3	63	0.27	0.0006	0.86	529,056	4,923,143	26,671	−32	291			
		Sour Creek	sill						549,238	4,937,400	14,503	−7	911			
		Mallard Lake						mean	528,819	4,923,362	20,537	−26.67				
								SD	205	465	2,870	4.24				
		Sour Creek						mean	550,394	4,936,440	13,801	−10.00				
								SD	1,911	1,126	965	3.00				

[a]*N*: number of data points; χ^2_ν: chi square per degrees of freedom, see (1). % 1StD: percentage of points with misfit smaller than 1 standard deviation. NMRSE: normalized root-mean-square error, see (A3) in Appendix S1; R^2: coefficient of determination, see (A4) in Appendix S1. *X* and *Y*, source location; ΔV: volume change; *A*: aspect ratio; θ: dip angle; φ: strike angle; SD: standard deviation. The best fit source in italics. Errors are 1 standard deviation.

mentioned cross-correlation analysis. While the macroareas within the caldera (ML and SC, and NCR) exhibit strongly nonlinear deformation time series over the 1992–2010 time interval (see also the displacement time series *R*-squared map reported in Figure 2b), the deformation trend of the SRP macroarea is practically linear with a mean rate of about 1 cm/yr in LOS.

For what concern the nonlinear deformation behavior, we were able to identify four time spans in which deformation within the caldera can be assumed quasi-linear over a properly identified set of pixels: 1992–1995, 1996–2003, 2004–2008, and 2009–2010. The maps shown in Figures 3c1–3c4 portray the spatial distribution of coherent pixels (value for the displacement time series *R*-squared greater than 0.8) for these four time periods. The mean deformation velocity maps are shown in Figures 3d–3g.

2.3. Removal of Secular Deformation

We removed the mean displacement rate of the northern sector of the SRP from the velocity maps (Figure 2a). This displacement rate is the result of tectonic processes controlled by interactions between the North American Plate, moving in the ENE–WSW direction with a rate of about 2 cm/yr, and the flow of the asthenospheric plume beneath the Yellowstone volcanic region [*DeNosaquo et al.,* 2009], a deformation pattern confirmed by available GPS measurements (Figure 4). We estimated the SRP average regional deformation rate by using the mean velocity values derived by the 1992–2010 deformation time series of the coherent SAR pixels belonging to the Snake River area (blue dots in Figure 3a). The detrended mean deformation velocity maps for the ML and SC resurgent domes and the NCR macroareas are shown in Figures 5 and 6, respectively.

2.4. Deformation Trends

According to our analysis, a general phase of subsidence (more precisely, an increase in the range distance) marked the caldera and the surrounding regions during the 1992–1995 time interval (Figures 5e and 6e), with the highest rates of deformation (about 3 cm/yr) recorded in the region of the resurgent domes. This trend is consistent with the process of caldera floor subsidence active since 1986 [*Dzurisin et al.,* 2012].

Beginning in 1996, the area close to the NCR began to uplift with rates of about 1.5 cm/yr (Figure 6f). Uplift was over in 2003, and this area has been subsiding with rates of 2–3 cm/yr (Figure 6g).

From 2004 to 2008, the InSAR measurements reveal a significant uplift of the resurgent domes region with rates up to 4 cm/yr (Figure 5g). Between the end of 2009 and the beginning of 2010, the caldera central floor has been experiencing a new phase of subsidence with a rate of ~1 cm/yr, slower than that of the 1992–1995 time interval (~3 cm/yr; Figure 5h). This trend is also confirmed by continuous GPS observations [*Chang et al.,* 2010].

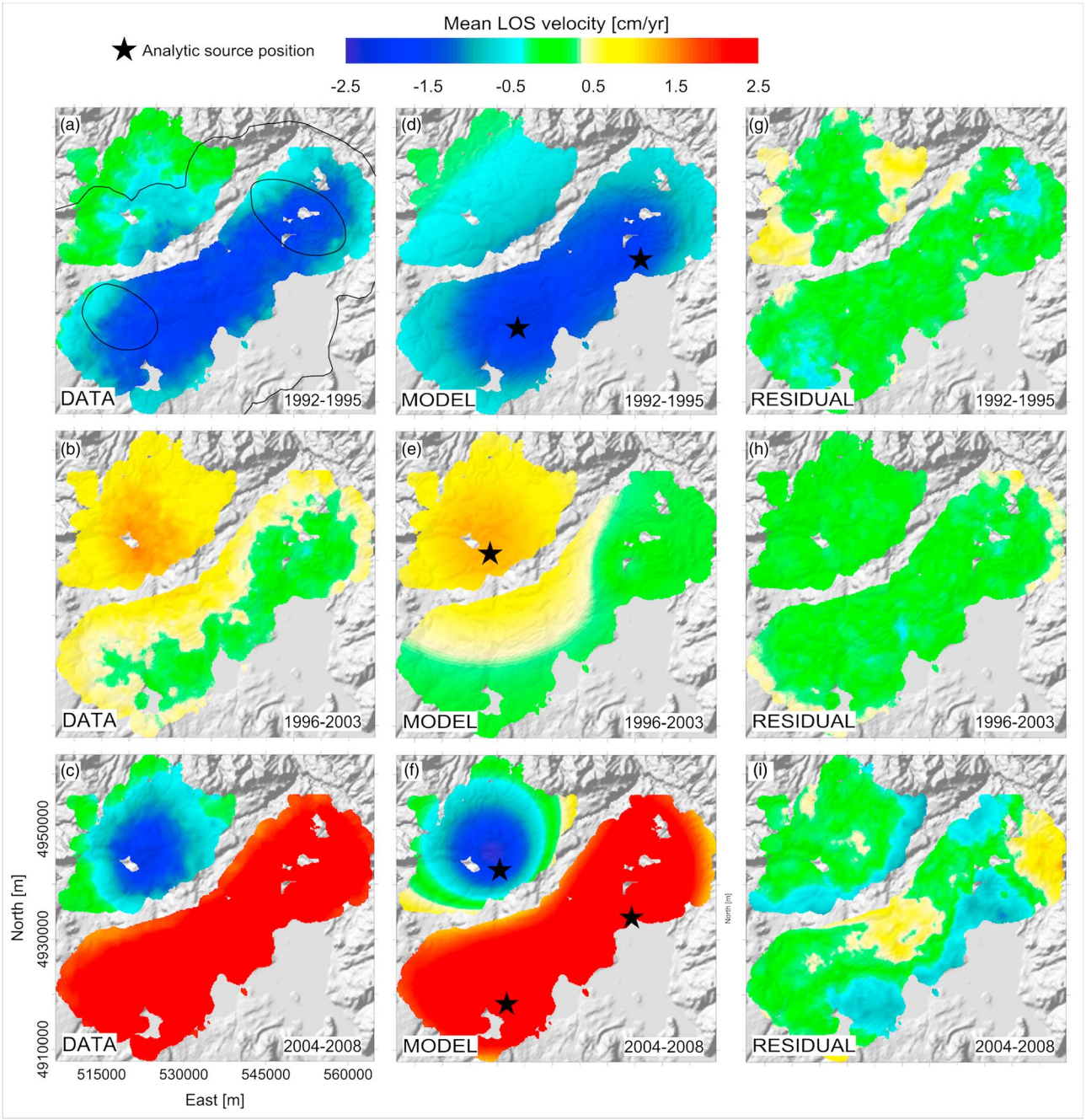

Figure 7. Misfit deformation data-model analysis. Comparison between modeling results and deformation retrieved through the SBAS differential InSAR analysis. (a–c) Data, (d–f) model, and (g–i) residual. (top row) 1992–1995, (middle row) 1996–2003, and (bottom row) 2004–2008. No significant deformation was measured for 2009–2010. In Figure 7a the black solid lines represent the caldera and resurgent dome boundaries (see Figure 1). In order to increase the spatial density measurements and minimize noise effect, we have performed an Inverse Distance to a Power (IDP) geospacing technique [*Davis*, 1986].

3. Modeling of InSAR Measurements

We employed the software dMODELS [*Battaglia et al.*, 2013] to find the best fit deformation sources. A number of sources (sphere, spheroid, and sill like) are available in dMODELS for several geodetic techniques: leveling, tilt, GPS, and InSAR. In the case of InSAR measurements, the software models the changes in range along the radar LOS. Although actual volcanic sources are not embedded cavities of simple shape, we assume that these models may reproduce the stress field created by the actual magma intrusion or hydrothermal fluid injection. The dMODELS software employs a nonlinear inversion algorithm to determine the best fit

Table 3. InSAR: Best Fit Source for 1996–2003[a]

N	P	Area	Geometry	χ^2_v	%	NRMSE 1StD	Residuals Analysis Mean	Residuals Analysis R^2	X (UTM)	Y (UTM)	Depth (m)	ΔV (10^6 m^3)	Radius (m)	A	θ (deg)	φ (deg)
27.292	*4*	*Northern Rim*	*sphere*	*0.5*	*84*	*0.09*	*0.0000*	*0.83*	*523,800 ±1,000*	*4,940,800 ±1,000*	*21,100 ±6,200*	*27 ±4*				
27.292	7	Northern Rim	spheroid	1.9	49	0.21	0.0010	0.87	522,012	4,942,846	16,738	19		1	0	312
27.292	5	Northern Rim	sill	0.6	82	0.11	0.0003	0.86	523,654	4,941,742	28,950	3	520			

[a]*N*: number of data points; χ^2_v: chi square per degrees of freedom, see (equation (1)). % 1StD: percentage of points with misfit smaller than 1 standard deviation. NMRSE: normalized root-mean-square error; see equation (A3) in Appendix S1; R^2: coefficient of determination, see equation (A5) in Appendix S1. *X* and *Y*, source location; Δ*V*: volume change; *A*: aspect ratio; θ: dip angle; φ: strike angle. The best fit source in italics. Errors are 1 standard deviation.

parameters for the deformation source by searching the minimum of the following cost function [*Battaglia et al.,* 2013]:

$$\chi^2_v = \frac{1}{N-P}\sum_{k=1}^{N}\left(\frac{d_k - m_k}{\sigma_k}\right)^2, \quad (1)$$

where *N* is the number of data points, *P* the number of model parameters, d_k are the experimental data, m_k the modeling results, and σ_k the data uncertainties (see also Appendix S1). The nonlinear inversion algorithm is a combination of local optimization (interior-point method [*Bonnans et al.,* 2006]) and random search. This approach is more efficient for hyper-parameter optimization than trials on a grid [*Bergstra and Bengio*, 2012]. When more than one source was causing the deformation (e.g., 1992–1995; Table 2), we run a simultaneous inversion for two geometric sources. Moreover, when the caldera deformation required the modeling of sources with opposite behavior (e.g., in 2004–2008 two sources were inflating, while a third one was deflating; see Figures 5g and 6g), we employed a strategy of successive approximations. For instance, for the 2004–2008 deformation, we (i) modeled first the uplift sources only, (ii) computed the deformation caused by the inflating sources for the whole caldera, (iii) subtracted this deformation from the InSAR signal, (iv) used the deformation from (iii) to model the deflating source beneath the NCR only, and (v) computed the total deformation caused by the superposition of the three active sources and compared the result against the InSAR signal.

The results of the InSAR measurements inversion and the locations of the different deformation sources are shown in Figure 7 and Tables 2–4. The inversion models reveal a substantial stability of the deformation sources beneath the resurgent domes (see Tables 2–4) over the considered time interval; a prolate spheroid is

Table 4. InSAR: Best Fit Sources for 2004-2008 (Figure 7c)[a]

N	P	Area	Geometry	χ^2_v	%	NRMSE 1StD	Residuals Analysis Mean	Residuals Analysis R^2	X (UTM)	Y (UTM)	Depth (m)	ΔV (10^7 m^3)	radius (m)	A	θ (deg)	φ (deg)
37.603	8	Mallard Lake	sphere	6.4	34	0.53	−0.008	0.69	526,595	4,918,051	18,167	6.10				
		Sour Creek	sphere						550,784	4,938,501	16,335	4.46				
37.603	*14*	*Mallard Lake*	*spheroid*	*3.6*	*34*	*0.49*	*−0.007*	*0.705*	*526,700 ±100*	*4,917,900 ±400*	*18,500 ±3400*	*50 ±5*		*0.44*	*11*	*333*
		Sour Creek	*spheroid*						*547,900 ±1,700*	*4,940,800 ±1,300*	*16,600 ±3,100*	*56 ±10*		*0.47*	*44*	*147*
37.603	10	Mallard Lake	sill	5.7	33	0.46	−0.007	0.71	526,578	4,918,673	24,189	6	601			
		Sour Creek	sill						550,828	4938501	11,110	4	20,280			
27.289	4	Northern Rim	sphere	3.1	48	0.23	0.0019	0.35	525,456	4,942,149	12410	−28				
	7		spheroid	3.7	45	0.16	0,0013	0.35	525863	4942291	11038	−24		1	23	297
	20		sill	3.2	46	0.05	−0,0001	0.21	525,300 ±300	4,943,000 ±500	18,000 ±3,700	−28 ±2	302			

[a]*N*: number of data points; χ^2_v: chi square per degrees of freedom, see (equation (1)). % 1StD: percentage of points with misfit smaller than 1 standard deviation. NMRSE: normalized root-mean-square error; see equation (A3) in Appendix S1; R^2: coefficient of determination; see equation (A5) in Appendix S1. *X* and *Y*, source location; Δ*V*: volume change; *A*: aspect ratio; θ: dip angle; φ: strike angle. The best fit source in italics. Errors are 1 standard deviation.

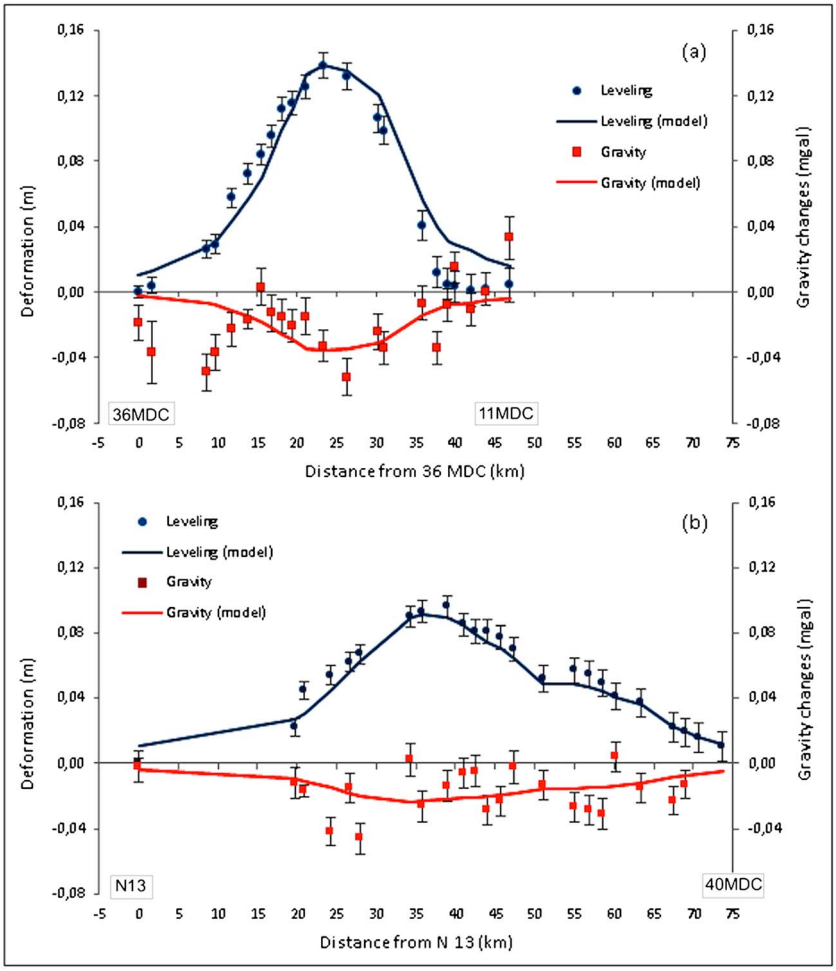

Figure 8. Leveling and gravity changes from 1977 to 1986. (a) Cumulative vertical displacements and gravity changes from 1977 to 1983 along the leveling route from Canyon Junction to Fishing Bridge Junction. This line runs just west of the SC resurgent dome (Figure 1). (b) Cumulative vertical displacements and gravity changes from 1977 to 1986 along the leveling route from Madison Junction to West Thumb Junction. This line runs west of ML resurgent dome (Figure 1). Data from *Arnet* [1996] and *Dzurisin et al.* [2012]; error bars are 1 standard deviation. See modeling results in Table 6.

the best fitting source geometry both during uplift and subsidence. On the other hand, deformation at the NCR zone is controlled by sources with different geometries. Inversion results reveal the existence of two deflation spheroid sources beneath the SC and ML resurgent domes from 1992 to 1995.The time interval from 1996 until 2003 is characterized by (i) the inflation of a spherical source in the NCR area and (ii) a quiescent state at the resurgent domes. Finally, between 2004 and 2008, the reverse in the trend of ground deformation (see Figures 3e and 3f) requires (i) the reactivation of the spheroidal sources beneath SC and ML resurgent domes macroareas and (ii) the transformation of the source beneath the NCR from an inflating sphere to a deflating sill.

4. Leveling and Gravity Measurements

We integrate our analysis with additional information from leveling and gravity measurements. In particular, we model gravity and uplift measurements collected between 1977 and 1993 from the two leveling routes shown in Figure 1 [*Arnet*, 1996; *Arnet et al.,* 1997; *Dzurisin et al.,* 2012]. Unfortunately, to the best of our knowledge, gravity data collected after 1993 have not been published yet.

Geodetic measurements in Yellowstone began in 1923, when the U.S. Coast and Geodetic Survey conducted initial leveling surveys along second-order lines in Yellowstone National Park to upgrade the vertical control

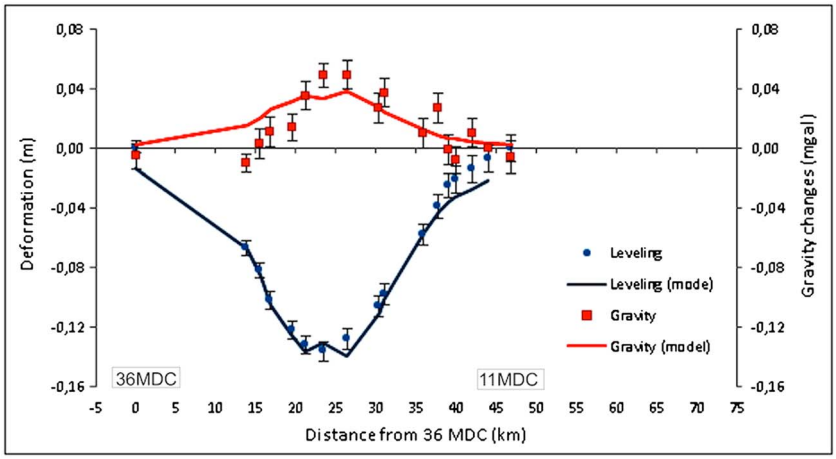

Figure 9. Leveling and gravity measurements from 1983 to 1993. Cumulative vertical displacements and gravity changes from 1983 to 1993 along the leveling route from Canyon Junction to Fishing Bridge Junction. This line runs just west of the SC resurgent dome (Figure 1). Data from *Arnet* [1996] and *Dzurisin et al.* [2012]; error bars are 1 standard deviation. See modeling results in Table 6.

network in the Yellowstone region [*Pelton and Smith,* 1979, 1982]. The U.S. Geological Survey, under the guidance of the University of Utah, surveyed the Yellowstone leveling network from 1976 to 2007 [*Dzurisin et al.*, 2012], following the *Federal Geodetic Control Committee* [1984] guidelines for first-order, class II surveys (see Appendix S2).

Leveling measurements show two main deformation episodes between 1977 and 1993: caldera uplift between 1977 and 1983 and caldera subsidence from 1983 to 1993 (Figures 8 and 9) with a transition period in 1984–1985. The results of the 1984 survey indicated that the area near the SC dome rose as much as +17.7 ± 0.6 cm during 1976–1984 at an average rate of +2.2 ± 0.1 cm/yr. The 1985 leveling survey indicated that the caldera vertical displacement from September 1984 to September 1985 was essentially zero. The 1986 survey showed that the SC dome had subsided about −2.5 ± 0.5 cm, the first documented occurrence of caldera floor subsidence in Yellowstone. Leveling surveys across the SC dome carried out each September from 1988 to 1993, showed progressive subsidence at rates that ranged from −1.1 ± 0.5 cm/yr to −3.2 ± 0.55 cm/yr [*Dzurisin et al.,* 2012].

The Yellowstone gravity network, established in 1977 by the University of Utah [*Smith et al.,* 1978], was reobserved in 1983 and 1993 [*Arnet*, 1996]. The characteristics of the gravity campaigns are summarized by *Arnet et al.* [1997]. Although the network consists of more than 150 stations spanning the whole caldera [*Arnet et al.,* 1997], the number of data points that can be actually employed in our analysis is limited by the availability of colocated leveling benchmarks [*Smith et al.,* 1978] that can be used to correct the gravity measurements for the free-air effect (Table S2). This constrain reduces the number of effective gravity data points to 46 for the uplift period (22 for the Canyon Junction-Fishing Bridge Junction leveling route between 1977 and 1983 and 24 for the Madison Junction-West Thumb Junction leveling route between 1977 and 1986) and 17 for the subsidence period (Canyon Junction-Fishing Bridge Junction leveling route between 1983 and 1993); see Figure 1, Table S2, Figures 8 and 9, and *Arnet* [1996].

Table 5. Comparison Between InSAR and Leveling Inversion[a]

			X	σ_x	Y	σ_Y	Depth	σ_D	ΔV	σ_V			θ	σ_θ	φ	σ_φ
Period	N	χ^2_v	(UTM)		(UTM)		(m)		(10^6 m^3)		A	σ_A	(deg)		(deg)	
1992–1995	48	1.1	547,800	1,600	493,7100	1,500	12,800	2,600	−35	6	0.32	0.19	35	36	301	92
1992–1995	15.316	0.9	552,600	1,900	4,935,200	1,100	12,700	1,000	−10	3	0.33		48		310	
Difference			−4,800	2,500	1,900	1,900	100	2,800	−25	7						

[a]The 1992–1995 deformation at Sour Creek dome is modeled using a spheroidal source. This area is the only part of the caldera monitored by both leveling and InSAR. The uncertainty modeling results of leveling is to equal to 2 standard deviation. N: data points; X and Y, source location; ΔV: volume change; A: aspect ratio; θ: dip angle; φ: strike angle.

Table 6. Location, Depth, Volume Change, and Density of Active Sources in Yellowstone Caldera From 1977 to 1986[a]

Time Lapse	Years	Data Set	X (UTM)	σ_x (m)	Y (UTM)	σ_y (m)	Depth (m)	σ_d (m)	ΔV (10^6 m^3)	σ_V (10^6 m^3)	ρ (kg/m^3)	σ_ρ (kg/m^3)
						Sour Creek Dome						
1	*1977-83*	*Leveling*	*547,100*	*3,200*	*4,941,000*	*2,900*	*5,900*	*3,000*	*54*	*36*	*800*	*600*
2	1983-93	Leveling	545,200	3,400	4,939,400	3,500	7,800	3,800	−67	56	1,500	900
						Mallard Lake Dome						
1 and 2	*1977–1986*	*Leveling*	*520,500*	*3,700*	*4,923,200*	*2,500*	*9,100*	*3,300*	*67*	*33*	*2,600*	*700*

[a]Italic font highlights inflation periods. The uncertainty is to equal to 1 standard deviation.

5. Modeling Leveling and Gravity Measurements

Yellowstone caldera deformation has been interpreted as the effect of either magma intrusion into the upper crust [e.g., *Wicks et al.,* 2006; *Chang et al.,* 2007, 2010; *Puskas et al.,* 2007] or a combination of hydrothermal fluid injection within the caldera hydrothermal system [e.g., *Pelton and Smith*, 1982; *Dzurisin et al.,* 1999]. The combined exploitation of geodesy and gravity measurements can allow us to infer the density of the intrusive fluids, and better constrain the deformation source [*Battaglia and Hill*, 2009]. Given the significant density difference between silicate melts (≈2500 kg/m^3) and hydrothermal fluids (≈1000 kg/m^3), it is reasonable to use density estimates from gravity to distinguish between these two possible sources of caldera unrest.

When trying to combine geodesy and microgravity to study the physics of active volcanoes, there are several issues that need to be addressed. The measured gravity changes Δg are the superposition of several effects [*Battaglia and Hill*, 2009]:

$$\Delta g = \gamma h + \Delta g_{\mathrm{WT}} + \Delta g_D + \Delta g_R. \tag{2}$$

The free-air effect is proportional to the uplift h ($\gamma = -0.3086$ mGal/m is the free-air gradient); the water table correction ($\Delta g_{\mathrm{WT}} = 0.04\varphi\delta z$ mGal) is proportional to the porosity φ and water table change δz (in meters) of an unconfined aquifer; Δg_D takes into account coupling effects between gravity and elastic deformation. The residual gravity Δg_R is the contribution depending on the mass change accompanying the deformation.

To estimate the residual gravity and, therefore, the mass of the intrusion during the observation periods, we removed from observed gravity measurement the noise from the free-air effect, the water table and the coupling between gravity and elastic deformation. We estimated the free-air correction using the uplift data available in Table S2. Since there are no direct measurements of the water table in Yellowstone Caldera, we used measurements of the level of Yellowstone Lake as a proxy of the changes in the level of the water table [*Farnes*, 2002], at least for the gravity sites in the vicinity of the lake. According to the data presented in Table S3, if we assume a porosity of 20% for the outcrops close to Yellowstone Lake, the water table contribution to the gravity signal is between 0.000 and 0.009 mGal and can be assumed practically negligible. Finally, the deformation effect Δg_D is negligible for spheroidal sources [*Battaglia and Hill*, 2009].

A critical step in the modeling of vertical deformation is the correct identification of the source geometry, since one dimensional deformation measurements can be satisfactorily fitted by more than one source [*Dieterich and Decker*, 1975]. We exploit the results of the InSAR measurements modeling (see section 3) to identify the deformation source geometries beneath the resurgent domes. InSAR LOS measurements are still one-dimensional measurement of deformation, but their very large spatial density can provide much better bounds on the source geometry. Inversion results show that deformation in the resurgent domes area is controlled by spheroidal sources and that this type of geometry remains substantially the same from 1992 to 2008 (see Tables 2–4). We employed the availability of both InSAR and leveling measurements at SC resurgent dome from 1992 to 1995 to verify the validity of our assumption. Accordingly, we have separately inverted the two sets of ground deformation measurements at SC using a spheroidal source. The results, shown in Table 5, indicate that the center location, depth, aspect ratio, and spatial orientation parameters of the two spheroidal sources recovered by the inversion of leveling or InSAR measurements are very similar within the 2 standard deviations confidence level.

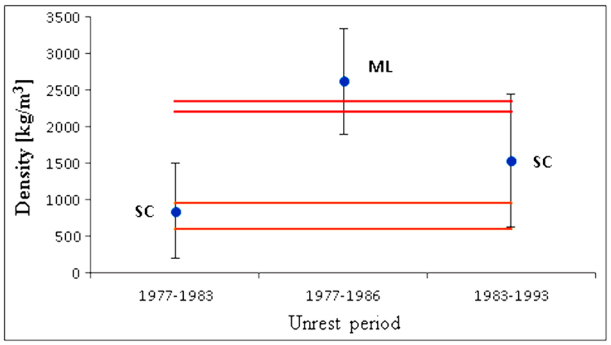

Figure 10. Density variations from 1977 to 1993. Density values of modeled deformation sources beneath SC dome = 1977–1983 (uplift), 1983–1993 (subsidence), and ML dome = 1977–1986 (uplift). The red and orange lines represent the density range of rhyolitic melts with a content of dissolved water between 1 and 4 wt % and hydrothermal system fluids, respectively. Error bars are 1 standard deviation. The value of the source density beneath SC for 1977–1983 suggests the intrusion of hydrothermal fluids. The density value for the source beneath ML supports the possibility of magma intrusion. The density range for the source beneath SC dome for 1983–1993 falls between a hydrothermal and silicate fluids and could indicate either a hybrid source (aqueous and silicate fluids) or a hydrothermal brine with a large percentage of salts dissolved in it [*Fournier*, 1989].

We estimated the source parameters (including the density of the intrusion) through a nonlinear joint inversion of leveling and gravity measurements, using a prolate spheroid. This modeling approach approximates the volume and mass change of the real source with the volume and mass change of a fluid-filled cavity [*Dvorak and Dzurisin*, 1997]. This approximation is a standard in volcano geodesy and has been successfully employed to study unrest at other calderas [e.g., *Battaglia et al.,* 2006]. The nonlinear inversion algorithm employs a combination of interior-point method [*Bonnans et al.,* 2006] and random grid search [*Bergstra and Bengio*, 2012] to find the minimum of the cost function:

$$\chi_v^2 = \frac{1}{N-P}\left(\vec{r_L}\cdot W_L \vec{r_L} + \vec{r_g}\cdot W_g \vec{r_g}\right), \quad (3)$$

where N is the number of data points (gravity and leveling), P the number of model parameters (a total of 15, 7 for the geodetic source, and 8 for the gravity sources), $\vec{r_L}$ the vector of residual for leveling, W_L the full covariance matrix for leveling (Appendix S2) [*Arnadottir et al.*, 1992], $\vec{r_g}$ the vector of residual for the residual gravity, and W_g the diagonal covariance matrix for residual gravity (see Table 6 for inversion results). It is worth noting that the density is directly computed as an independent parameter of the function modeling the gravity change for a spheroid.

We used bootstrap to estimate the uncertainties of the model parameters [*Johnson*, 2001]. Bootstrap is a procedure that involves choosing random samples with replacement from the original data set and inverting each sample the same way. By repeating this procedure a large number of times, we can assign an uncertainty (defined in terms of standard deviation) to sample estimates. Sampling with replacement means that every sample is returned to the data set after sampling. So a particular data point from the original data set could appear multiple times in a given bootstrap sample. The number of elements in each bootstrap sample equals the number of elements in the original data set. For example, to estimate the uncertainties of the source parameters (including the density) for this problem, we first run the joint inversion of gravity and uplift, randomly resampling the data set, for 250 times. Then we used the standard deviation of the 250 bootstrap inversions to assign an uncertainty to our parameters (Table 6).

Modeling results for the joint inversion of leveling and gravity measurements are available in Table 6 and Figures 8 (leveling and gravity between 1977 and 1986), 9 (leveling and gravity after 1983), and 10 (density). Figures 8 and 9 show a comparison between field measurements and best fit models. We can see that the spheroidal model fits the leveling measurements better than the gravity measurements, in particular for a section of the leveling route approximately 1 km east of Yellowstone Lake (sites 35 MDC, 34 MDC, and D12; see Figure B14 in *Dzurisin et al.* [2012]). There may be several reasons for this misfit: gravity measurements are usually much more noisy than leveling measurements [e.g., see *Battaglia and Hill*, 2009, Figure 7]; gravity measurements may have been influenced by local changes in the water table that we were not able to model; finally, there may be more than one source influencing the gravity measurements but not the leveling measurements. We would like to stress that all measurement points have been employed in the inversion. The presence of these misfit measurements is reflected in the larger uncertainties for the density and volume.

The results indicate that the depths of the sources range from 9000 ± 4000 m to 6000 ± 3000 m, the volume change from $(-67 \pm 56) \cdot 10^6$ m^3 (source deflation) to $(67 \pm 33) \cdot 10^6$ m^3, and the density of the deformation sources which spans between 800 ± 600 kg/m^3 (hydrothermal fluid) and 2600 ± 700 kg/m^3 (a rhyolite), with

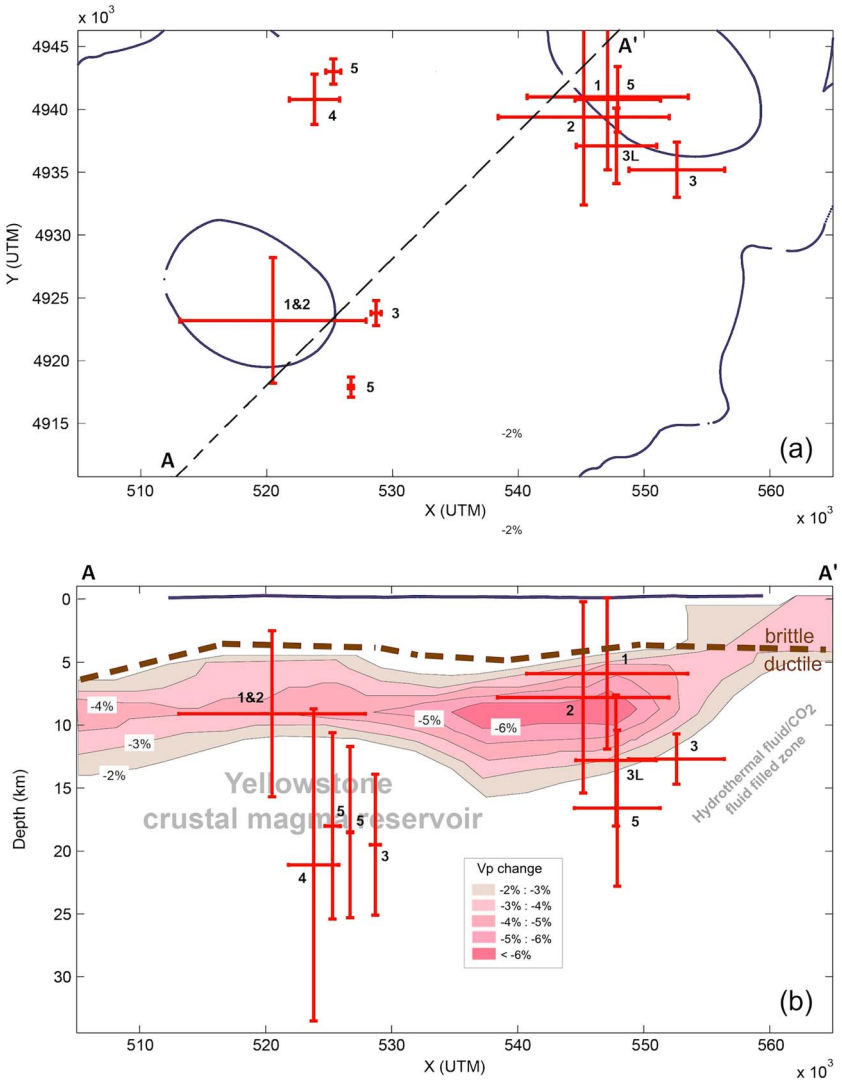

Figure 11. Location and depth of deformation sources. Error bars are 2 standard deviations. (a) Sources location; blue lines are the caldera rim and domes. The A-A′ dashed black line is the location of the cross section in the bottom panel. (b) Sources depth superimposed over the % V_P change contour map (after *Farrell et al.* [2014]); the dark blue line is the caldera altitude profile. The dashed brown line is the brittle-ductile transition zone (4 to 6 km deep [*DeNosaquo et al.*, 2009]). The contour plot in the background shows the relative change in the V_P velocity; see also Figure 12. Label corresponds to the time lapse: 1 = 1977–1983 (leveling), 2 = 1983–1993 (leveling), 1 and 2 = 1977–1986 (leveling); 3 = 1992–1995 (InSAR), 3L = 1992–1995 (leveling); 4 = 1996–2003 (InSAR), 5 = 2004–2008 (InSAR); see Tables 2–4 and 6 for modeling results. Note: Datum for geodetic inversion (average topography, 2500 m above sea level) has been shifted to be consistent in this plot with the datum for seismic tomography (sea level).

uncertainties taken equal to one standard deviation. Moreover, we locate the source below the brittle-ductile transition zone that in Yellowstone is at a depth between 4 and 6 km under the resurgent domes area [*DeNosaquo et al.,* 2009]. In particular,

1. The source beneath SC dome for the uplift period (1977–1983) is 6000 ± 3000 m deep with a density of 800 ± 600 kg/m^3; the value of the density and the depth of the source suggest the intrusion of hydrothermal fluids (Figure 10) at the base of the caldera hydrothermal system [*Hurwitz and Lowenstern*, 2014];
2. The source beneath ML dome (1977–1986; uplift from 1977 to 1984 and subsidence from 1985 to 1986) is 9000 ± 3300 m deep and has a density of 2600 ± 700 kg/m^3; the density value and source depth (below the brittle-ductile transition zone; see *DeNosaquo et al.* [2009]) supports the possibility of an intrusion of magma beneath the resurgent dome (Figure 10);

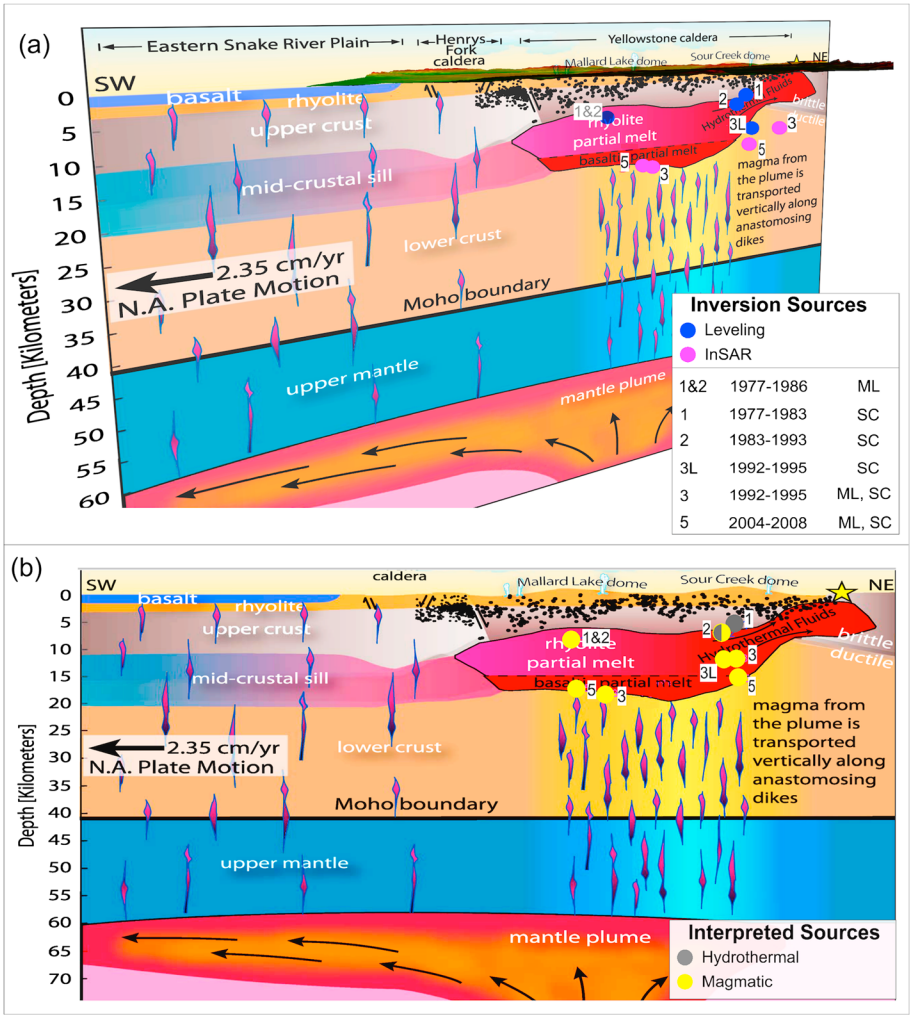

Figure 12. Interpretation model of Yellowstone caldera. (a) Location and depth of deformation sources at resurgent domes against the caldera interpretation seismic tomography model generated by *Farrell et al.* [2014], along the cross section identified by the A-A′ dashed black line in Figure 11a. The yellow star is the location of the Hot Springs Basin Group. (b) Below are reported the orthogonal projections of the sources on the interpreted section. Labels 1 and 2, 1, 2, 3L, 3, and 5 are the same as in Figure 11.

3. The source beneath SC dome for the subsidence period of 1983–1993 is 8000 ± 4000 m deep and has a density of 1500 ± 900 kg/m^3; the density value falls between a hydrothermal and silicate fluids and could indicate either an enrichment of the magmatic component or a hydrothermal brine with a large percentage of salts dissolved in it (Figure 10) [*Fournier*, 1989].

6. Results Interpretation and Conclusions

The inversion of the InSAR, leveling, and gravity measurements allows us to investigate the multiple episodes of ground deformation (uplift and subsidence) which affected Yellowstone Caldera during the last three decades. In particular, our analysis shows that the deformation sources responsible for the caldera unrest are concentrated in three distinct areas (Figure 3): (i) Mallard Lake (ML) dome (ii), Sour Creek (SC) dome, and (iii) the Northern Caldera Rim area (NCR). All deformation sources are most probably located below the brittle-ductile transition zone that in Yellowstone is at a depth between 4 and 6 km under the resurgent domes area [*DeNosaquo et al.*, 2009] and between 7 and 9 km in the northern caldera/Norris Geyser Basin region [*Smith et al.*, 2009] (Figure 11). It is worth noting that even the two sources closer to northern

Table 7. Summary of Deformation Sources Active in Yellowstone Caldera From 1977 to 2010[a]

Time lapse	Years	Geodetic data	Deformation macro-areas		
			Sour Creek dome	Mallard Lake dome	Northern Rim
1	1977-83	Leveling	**spheroid**	**spheroid**[b]	no leveling data
2	1983-93	Leveling	spheroid		
3a	1992-95	Leveling	spheroid	no leveling data	
3b	1992-95	InSAR	spheroid	spheroid	
4	1996-03	InSAR			**sphere**
5	2004-08	InSAR	**spheroid**	**spheroid**	sill
6	2009-10	InSAR			

[a]The grey background identifies area/years with no significant deformation measured by InSAR (signal within the background noise). Sources in bold font are inflating.
[b]The time period investigated is from 1977 to 1986.

caldera/Norris Geyser Basin region (source 4 and 5; Figure 11) are at depths well below the depth of the brittle-ductile transition zone (see Tables 3 and 4).

We interpret our InSAR (Figures 5–7) and leveling/gravity (Figures 8–10) inversion results in the light of the existing seismic tomography studies [*Husen et al.,* 2004; *Farrell et al.,* 2014]. In particular, in Figures 11 and 12 we have superimposed our inversion solutions over a section of the seismic tomography models by *Farrell et al.* [2014]. Inversion results for the first uplift episode of the ML dome between 1977 and 1986 (time lapses 1 and 2) retrieve a density of 2600 ± 700 kg/m^3 (Figure 10) and a source depth of 9000 ± 3000 m (Table 6), within the rhyolite partial melt zone (see Figure 12). These results indicate that magma migration into the upper crust is the most probable cause of the uplift at the ML dome.

The uplift of the SC dome from 1977 to 1983 (time lapse 1) was caused by a shallower source (6000 ± 3000 m deep, Table 6) with a density of 800 ± 600 kg/m^3 (Figure 10). These values are consistent with a hydrothermal fluids source. Again, this is in agreement with the interpretation of the tomographic results by *Farrell et al.* [2014]; see Figure 12. If volatiles, exsolved from magma beneath the caldera, are trapped temporarily beneath a self-sealing layer, the resulting pressurization can contribute to the surface uplift [*Fournier*, 1989].

The later subsidence of the SC dome from 1983 to 1993 (time lapse 2) is associated to a deeper source (8000 ± 4000 m; see Table 6) and a density increase to 1500 ± 900 kg/m^3 (Figure 10). We interpret these results as the effect of the migration of the source toward a region beneath the caldera with a more predominant presence of partial melt (see Figure 12).

The inversion of InSAR and leveling measurements belonging to the 1992–1995 interval (time lapse 3 and 3L) consistently show a deepening of the deformation sources located beneath the SC dome, an indication that magmatic component of the source may have become more significant. This trend is further emphasized by the inversion of the 2004–2008 (time lapse 5) deformation. In particular, according to seismic tomography images [*Farrell et al.*, 2014], the sources responsible of the uplift (solution 5 in Figure 11) are confined at depth were the tomographic studies relevant to the % V_P perturbation indicates the location of the Yellowstone crustal magma reservoir (Figures 11 and 12).

With reference to the NCR zone, the 1996–2003 uplift is probably due to magma accumulation [*Wicks et al.,* 2006]. Moreover, the following (2004–2008) subsidence phase could be interpreted as either the result of magma/fluids migration outside the caldera [*Dzurisin et al.,* 2012] or as the effect of a gravitational adjustment of the source, evolved from a spheric to a sill-like geometry (Table 7). This interpretation is supported by the similar depths and volume changes inferred from our InSAR inversion results for these two periods (see Tables 3 and 4).

Hydrothermal fluids are the driving forces behind the uplift of the SC resurgent dome between 1977 and 1983. It is worth noting that since the 1983–1993 period, the SC deformation source has been transforming into a deeper, more magmatic one (Figure 12). For what concern the unrest at the ML resurgent dome, the density and depths from our solutions confirm the magmatic nature of the retrieved source (Figure 12) for the almost

30 years investigated in this work. In particular, the magmatic nature of this source could be the effect of the flow of magma batches from the mantle plume, migrated across the ductile region through a network of anastomosing dikes.

Acknowledgments
Leveling data from 1976 to 1995 from the University of Utah and the U.S. Geological Survey are available courtesy of D. Dzurisin (Cascades Volcano Observatory). Comments from C. Wicks (USGS), J. Lowenstern (USGS), D. Dzurisin (USGS), J. Farrell (University of Utah), and two anonymous reviewers greatly helped to improve the manuscript. We thank ESA for providing the SAR ERS and ENVISAT data within the Cat-1 Project 6311. Finally, we thank S. Guarino, F. Parisi, and M.C. Rasulo for their technical support. InSAR data can be requested—for non-commercial, research purposes only—to Pietro Tizzani. Leveling and gravity data employed for our analysis are in Table S2. Yellowstone Lake levels are in Table S3. The dMODELS software is free and can be downloaded from the USGS website: http://pubs.usgs.gov/tm/13/b1/.

References

Aly, M. H., and E. S. Cochran (2011), Spatio-temporal evolution of Yellowstone deformation between 1992 and 2009 from InSAR and GPS observations, *Bull. Volcanol.*, *73*, 1407–1419.

Arnadottir, T., P. Segall, and M. Matthews (1992), Resolving the discrepancy between geodetic and seismic fault models for the 1989 Loma Prieta, California, earthquake, *Bull. Seismol. Soc. Am.*, *82*, 2248–2255.

Arnet, F. (1996), Crustal deformation of the Yellowstone volcanic field from precise measurements of temporal gravity changes and supplementary leveling and GPS data, PhD thesis, Institut für Geodäsie und Photogrammetrie, Eidg. Technische Hochschule Zürich, Switzerland.

Arnet, F., H. G. Kahle, E. Klingele, R. B. Smith, C. M. Meertens, and D. Dzurisin (1997), Temporal gravity and height changes of the Yellowstone caldera, 1977–1994, *Geophys. Res. Lett.*, *24*, 2741–2744, doi:10.1029/97GL02801.

Bamler, R., and P. Hartl (1998), Synthetic aperture radar interferometry, *Inverse Probl.*, *14*, R1–R54.

Battaglia, M., and D. P. Hill (2009), Analytical modeling of gravity changes and crustal deformation at volcanoes: The Long Valley Caldera, California, case study, *Tectonophysics*, *471*, 45–57.

Battaglia, M., C. Troise, F. Obrizzo, F. Pingue, and G. De Natale (2006), Evidence for fluid migration as the source of deformation at Campi Flegrei Caldera (Italy), *Geophys. Res. Lett.*, *33*, L01307, doi:10.1029/2005GL024904.

Battaglia, M., P. F. Cervelli, and J. R. Murray (2013), dMODELS: A MATLAB software package for modeling crustal deformation near active faults and volcanic centers, *J. Volcanol. Geotherm. Res.*, *254*, 1–4, doi:10.1016/j.jvolgeores.2012.12.018.

Berardino, P., G. Fornaro, R. Lanari, and E. Sansosti (2002), A new algorithm for surface deformation monitoring based on small baseline differential SAR interferograms, *IEEE Trans. Geosci. Remote Sens.*, *40*, 2375–2383, doi:10.1109/TGRS.2002.803792.

Bergstra, J., and Y. Bengio (2012), Random search for hyper-parameter optimization, *J. Mach. Learn. Res.*, *13*, 281–305.

Bonano, M., M. Manunt, M. Marsella, and R. Lanari (2012), Long-term ERS/ENVISAT deformation time-series generation at full spatial resolution via the extended SBAS technique, *Int. J. Remote Sens.*, *33*, 4756–4783, doi:10.1080/01431161.2011.638340.

Bonnans, J. F., J. C. Gilbert, C. Lemaréchal, and C. A. Sagastizábal (2006), *Numerical Optimization: Theoretical and Practical Aspects*, xiv+490 pp., Springer, Berlin, doi:10.1007/978-3-540-35447-5.

Casu, F., M. Manzo, and R. Lanari (2006), A quantitative assessment of the SBAS algorithm performance for surface deformation retrieval from DInSAR data, *Remote Sens. Environ.*, *102*, 195–210.

Chang, W. L., R. B. Smith, C. Wicks, J. M. Farrell, and C. M. Puskas (2007), Accelerated uplift and magmatic intrusion of the Yellowstone Caldera, 2004–2006, *Science*, *318*, 952–956, doi:10.1126/science.1146842.

Chang, W. L., R. B. Smith, J. Farrell, and C. M. Puskas (2010), An extraordinary episode of Yellowstone caldera uplift, 2004–2010, from GPS and InSAR observations, *Geophys. Res. Lett.*, *37*, L23302, doi:10.1029/2010GL045451.

Christiansen, R. L. (2001), *The Quaternary and Pliocene Yellowstone Plateau Volcanic Field of Wyoming, Idaho, and Montana*, *U.S. Geol. Surv. Prof. Pap.*, *729-G*, 145 pp.

Costantini, M. (1998), A novel phase unwrapping method based on network programming, *IEEE Trans. Geosci. Remote Sens.*, *36*(3), 813–821.

Davis, J. C. (1986), *Statistics and Data Analysis in Geology*, John Wiley, New York.

DeNosaquo, K. R., R. B. Smit, and A. R. Lowry (2009), Density and lithospheric strength models of the Yellowstone–Snake River Plain volcanic system from gravity and heat flow data, *J. Volcanol. Geotherm. Res.*, *188*, 108–127.

Dieterich, J. H., and R. W. Decker (1975), Finite element modeling of surface deformation associated with volcanism, *J. Geophys. Res.*, *80*, 4094–4102, doi:10.1029/JB080i029p04094.

Dvorak, J. J., and D. Dzurisin (1997), Volcano geodesy: The search for magma reservoirs and the formation of eruptive vents, *Rev. Geophys.*, *35*, 343–384, doi:10.1029/97RG00070.

Dzurisin, D., J. C. Savage, and R. O. Fournier (1990), Recent crustal subsidence at Yellowstone caldera, Wyoming, *Bull. Volcanol.*, *52*(4), 247–270.

Dzurisin, D., K. M. Yamashita, and J. W. Kleinman (1994), Mechanisms of crustal uplift and subsidence at the Yellowstone caldera, Wyoming, *Bull. Volcanol.*, *56*(4), 261–270.

Dzurisin, D., Jr., C. Wicks, and W. Thatcher (1999), Renewed uplift at the Yellowstone Caldera measured by leveling surveys and satellite radar interferometry, *Bull. Volcanol.*, *61*, 349–355.

Dzurisin, D., C. W. Wicks, and M. P. Poland (2012), *History of Surface Displacements at the Yellowstone Caldera, Wyoming, From Leveling Surveys and InSAR Observations, 1923–2008*, *U.S. Geol. Surv. Prof. Pap.*, *1788*.

Farnes, P. E. (2002), Natural variability in annual maximum water level and outflow of Yellowstone Lake, in *Yellowstone Lake: Hotbed of Chaos or Reservoir of Resilience? Proceedings of the 6th Biennial Scientific Conference on the Greater Yellowstone Ecosystem. October 8–10, 2001, Mammoth Hot Springs Hotel, Yellowstone National Park*, edited by R. J. Anderson and D. Harmon, pp. 69–74, Hancock, Mich.

Farrell, J., R. B. Smith, S. Husen, and T. Diehl (2014), Tomography from 26 years of seismicity revealing that the spatial extent of the Yellowstone crustal magma reservoir extends well beyond the Yellowstone Caldera, *Geophys. Res. Lett.*, *41*, 3068–3073, doi:10.1002/2014GL059588.

Federal Geodetic Control Committee (1984), Standards and specifications for geodetic control networks, John D. Bossler, Chairman September 1984, Geodesy-Standards-United States. I. Bossler, John D. II. Title. QB296.U89U5 1984 526.3'3 84-600257, Rockville, Md.

Fornaro, G., G. Franceschetti, R. Lanari, D. Rossi, and M. Tesauro (1997a), Interferometric SAR phase unwrapping using the finite element method, *IEE Proc. Radar Sonar Navig.*, *144*, 266–274.

Fornaro, G., G. Franceschetti, R. Lanari, E. Sansosti, and M. Tesauro (1997b), Global and local phase-unwrapping techniques: A comparison, *J. Opt. Soc. Am. A*, *14*, 2702–2708.

Fournier, R. O. (1989), Geochemistry and dynamics of the Yellowstone National Park hydrothermal system, *Annu. Rev. Earth Planet. Sci.*, *17*, 13.

Franceschetti, G., and R. Lanari (1999), *Synthetic Aperture Radar Processing*, CRC Press.

Goldstein, R. M., H. A. Zebker, and C. L. Werner (1988), Satellite radar interferometry: Two dimensional phase unwrapping, *Radio Sci.*, *23*, 713–720, doi:10.1029/RS023i004p00713.

Hurwitz, S., and J. B. Lowenstern (2014), Dynamics of the Yellowstone hydrothermal system, *Rev. Geophys.*, *52*(3), 375–411, doi:10.1002/2014RG000452.

Husen, S., R. B. Smith, and G. P. Waite (2004), Evidence for gas and magmatic sources beneath the Yellowstone volcanic field from seismic tomographic imaging, *J. Volcanol. Geotherm. Res.*, *131*, 397–410.

Hutnak, M., S. Hurwitz, S. E. Ingebritsen, and P. A. Hsieh (2009), Numerical models of caldera deformation: Effects of multiphase and multicomponent hydrothermal fluid flow, *J. Geophys. Res.*, *114*, B04411, doi:10.1029/2008JB006151.

Johnson, R. W. (2001), An introduction to bootstrap, *Teach. Stat.*, *23*, 49–54.

Lanari, R., F. Casu, M. Manzo, G. Zeni, P. Berardino, M. Manunta, and A. Pepe (2007), An overview of the small baseline subset algorithm: A DInSAR technique for surface deformation analysis, *Pure Appl. Geophys.*, *164*, 637–661, doi:10.1007/s00024-007-0192-9.

Pelton, J. R., and R. B. Smith (1979), Recent crustal uplift in Yellowstone National Park, *Science*, *206*(4423), 1179–1182, doi:10.1126/science.206.4423.1179.

Pelton, J. R., and R. B. Smith (1982), Contemporary vertical surface displacements in Yellowstone National Park, *J. Geophys. Res.*, *87*, 2745–2761, doi:10.1029/JB087iB04p02745.

Pepe, A., and R. Lanari (2006), On the extension of the minimum cost flow algorithm for phase unwrapping of multitemporal differential SAR interferograms, *IEEE Trans. Geosci. Remote Sens.*, *44*(9), 2374–2383.

Pepe, A., E. Sansosti, P. Berardino, and R. Lanari (2005), On the generation of ERS/ENVISAT DInSAR time-series via the SBAS technique, *IEEE Geosci. Remote Sens. Lett.*, *2*, 265–269.

Pierce, K. L., K. P. Cannon, G. A. Meyer, M. J. Trebesch, and R. D. Watts (2002), *Post-Glacial Inflation-Deflation Cycles, Tilting, and Faulting in the Yellowstone Caldera Based on Yellowstone Lake Shorelines*, *U.S. Geol. Surv. Open File Rep.*, *2002-142*.

Puskas, C. M., R. B. Smith, C. M. Meertens, and W. L. Chang (2007), Crustal deformation of the Yellowstone–Snake River Plainvolcano-tectonic system: Campaign and continuous GPS observations, 1987–2004, *J. Geophys. Res.*, *112*, B03401, doi:10.1029/2006JB004325.

Rosen, P. A., S. Hensley, I. R. Joughin, F. K. Li, S. N. Madsen, E. Rodríguez, and R. M. Goldstein (2000), Synthetic aperture radar interferometry, *IEEE Trans. Geosci. Remote Sens.*, *48*, 333–382.

Rosen, P. A., S. Hensley, E. Gurrola, F. Rogez, S. Chan, and J. Martin (2001), SRTM C-band topographic data quality assessment and calibration activities, in *Proc. IGARSS*, pp. 739–741, Sydney, Australia.

Smith, R. B., J. R. Pelton, and J. A. Evoy (1978), Uplift and its relationship to mass deficiency at Yellowstone, *Eos Trans. AGU*, *59*(12), 1189.

Smith, R. B., M. Jordan, B. Steinberger, C. M. Puskas, J. Farrell, G. P. Waite, S. Husen, W. Chang, and R. O'Connell (2009), Geodynamics of the Yellowstone hotspot and mantle plume: Seismic and GPS imaging, kinematics, and mantle flow, *J. Volcanol. Geotherm. Res.*, *188*, 26–56.

Tizzani, P., P. Berardino, F. Casu, P. Euillades, M. Manzo, G. P. Ricciardi, G. Zeni, and R. Lanari (2007), Surface deformation of Long Valley Caldera and Mono Basin, California, investigated with the SBAS-InSAR approach, *Remote Sens. Environ.*, *108*, 277–289.

Vasco, D. W., R. B. Smith, and C. L. Taylor (1990), Inversion for sources of crustal deformation and gravity change at the Yellowstone Caldera, *J. Geophys. Res.*, *95*, 19,839–19,856, doi:10.1029/JB095iB12p19839.

Vasco, D. W., C. M. Puskas, R. B. Smith, and C. M. Meertens (2007), Crustal deformation and source models of the Yellowstone volcanic field from geodetic data, *J. Geophys. Res.*, *112*, B07402, doi:10.1029/2006JB004641.

Wicks, C., W. Thatcher, and D. Dzurisin (1998), Migration of fluids beneath Yellowstone Caldera inferred from satellite radar interferometry, *Science*, *282*, 458–462.

Wicks, C., W. Thatcher, D. Dzurisin, and J. Svarc (2006), Uplift, thermal unrest and magma intrusion at Yellowstone Caldera, *Nature*, *440*, 72–75.

Yang, Y., A. Pepe, M. Manzo, M. Bonano, D. N. Liang, and R. Lanari (2013), A simple solution to mitigate noise effects in time-redundant sequences of small baseline multi-look DInSAR interferograms, *Remote Sens. Lett.*, *4*, 609–618, doi:10.1080/2150704X.2013.771826.

Zebker, H. A., and J. Villasenor (1992), Decorrelation in interferometric radar echoes, *IEEE Trans. Geosci. Remote Sens.*, *30*, 950–959.